Structural characterization of tin nanocrystals embedded in silicon by atomic probe tomography

Soren Roesgaard, Etienne Talbot, Constantinos Hatzoglou, John Lundsgaard Hansen, Brian Julsgaard

Structural characterization of tin nanocrystals embedded in silicon by atomic probe tomography

Søren Roesgaard[1], **Etienne Talbot**[2], **Constantinos Hatzoglou**[2], **John Lundsgaard Hansen**[3] and **Brian Julsgaard**[1,3]

[1] Interdisciplinary Nanoscience Center (iNANO), Aarhus University, Gustav Wieds Vej 14, DK-8000 Aarhus C, Denmark
[2] Normandie Univ, UNIROUEN, INSA Rouen, CNRS, Groupe de Physique des Matériaux, 76000 Rouen, France
[3] Department of Physics and Astronomy, Aarhus University, Ny Munkegade 120, DK-8000 Aarhus C, Denmark

E-mail: brianj@phys.au.dk

Abstract

Tin nanocrystals embedded in silicon are studied by atom probe tomography and by photoluminescence spectroscopy in the 0.76–1.07 eV region of emission energies. The nanocrystals have been fabricated by molecular beam epitaxy followed by a post-growth annealing step at various temperatures. One particular sample, annealed at a temperature of 725 °C, shows a distinctly higher optical activity. It is found, however, that the distinct behavior cannot be explained by variations in the nanocrystal composition or in the properties of Sn atoms dissolved in the surrounding Si matrix, which can be investigated by atom probe tomography.

For quite some time, there has been a strong desire to integrate optical functionality in standard complementary metal-oxide-semiconductor (CMOS) devices based on silicon (Si). In Si-photonics the aim is to combine the electrical functionality of Si with the optical functionality offered by direct-bandgap materials. The merging of these functionalities has often been approached by combining the Si with group-III–V-based systems, which however tend to be chemically incompatible with Si [1]. Another approach is to obtain the optical activity from a monolithic implementation of group-IV alloys [2]. This is possible due to the direct-bandgap nature of tin (Sn) in its diamond-structured and semiconducting α-Sn phase. Lately, germanium-tin (GeSn) alloys have been used in the demonstration of light-emitting diodes [3] and lasing [4–6] at temperatures up to 180 K. Furthermore, a multistack GeSiSn/GeSn has shown similar lasing activity [7]. Such thin films are currently of great interest; however, there might be interesting possibilities in turning to embedded nanocrystals since the control of the nanocrystal diameter could constitute another handle for tuning the bandgap energy, and in turn, allow for tunable lasers [8]. Light emission from Si with embedded Sn nanocrystals has previously been presented, where the Sn nanocrystals were formed upon post-annealing of a solid solution of Sn in Si grown by molecular beam epitaxy (MBE) [9]. In that work, a significant increase in optical activity was found within a narrow annealing temperature window around 725 °C, although no structural difference between Sn nanocrystals formed at different annealing temperatures could be detected by electron microscopy. Recently, it was found, surprisingly, that the sample with the increased light emission contained nanocrystals in the metallic β-Sn phase [10], which is in contradiction to previous findings stating that Sn-nanocrystals smaller than ~8nm should be α-Sn [11]. The exact physical mechanism behind the light emission is still not understood, which calls for further investigation. In the present manuscript we use laser-assisted three-dimensional atom probe tomography (APT) to investigate if there are any differences in the composition of the Sn nanocrystals or the surrounding matrix that could be correlated to the optical properties of the nanocrystals. The APT method, which provides three-dimensional mapping of atoms in a material, has previously been used to understand nanoscale clustering and measure accurate composition of nano-objects in semiconductor or oxide materials. For example, the composition of rare-earth silicate nanoclusters was determined by APT allowing to identify the phase-separation mechanism of rare-earth doped silicon oxide and to explain the optical properties [12, 13]. By quantifying the Si-nanocluster

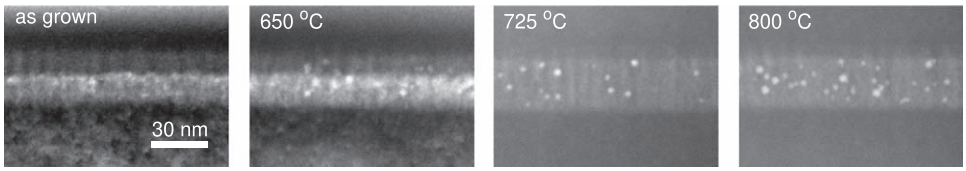

Figure 1. STEM images of the as-grown SiSnC layer and the Sn-nanocrystal-containing layers. The bright contrast is due to Sn atoms, seen either as a continuous band corresponding to the original SiSnC layer or as bright spots from individual Sn nanocrystals.

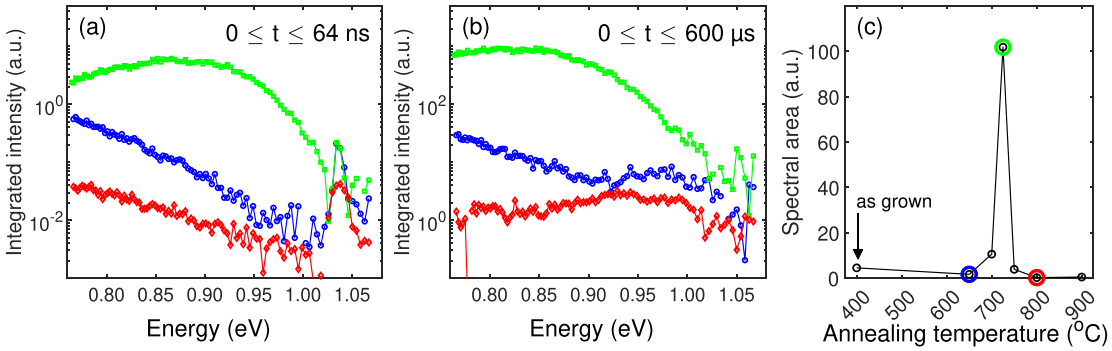

Figure 2. In all panels, samples annealed at temperatures of 650, 725, and 800 °C are color coded as blue, green, and red, respectively. (a) Time-integrated PL spectra for early times ($0 \leqslant t \leqslant 64$ ns). (b) Time-integrated PL spectra for late times ($0 \leqslant t \leqslant 600$ μs). (c) Integrated spectral area below each late-time spectra for emission energies in the range 0.76 eV $\leqslant E \leqslant$ 0.90 eV. The three specific annealing temperatures investigated here are marked by colored circles (see [9] for further information).

characteristics (size distribution, composition, etc) in silica using APT, Roussel *et al* have demonstrated the growth mechanism of Si-nanoclusters to depend on the supersaturation [14].

The samples investigated were grown by MBE. A composite layer of 30 nm thickness containing Si, Sn, and carbon (C) was evaporated onto a Si substrate, resulting in concentrations of 1.6% Sn and 0.04% C within the Si matrix, determined by secondary-ion mass spectrometry. The C was added in order to reduce the strain and suppress dislocations [15]. Post-growth annealing was carried out in a N_2 atmosphere at 650, 725, and 800 °C for 20 min in order to form the nanocrystals. Additional details are given in [9]. The resulting Sn-nanocrystals were investigated by scanning transmission electron microscopy (STEM) and the resulting images are shown in figure 1. The MBE-grown SiSnC layer together with the nanocrystals, formed upon post-annealing at temperatures $\gtrsim$600 °C [16], are clearly visible. The images also indicate a columnar structure of the grown layers for all temperatures including the as-grown sample.

The samples were characterized optically by photoluminescence (PL) spectroscopy, using excitation laser pulses of 100 fs duration, 400 nm wavelength, and 8×10^{-6} J cm^{-2} pump fluence. The samples were mounted in a cryostat and kept at a temperature of 16 K. The resulting PL spectra for the three samples annealed at different temperatures are shown in figure 2. The early-time integrated PL spectra, seen in figure 2(a), show a narrow peak centered around $\approx$1.035 eV, which is assigned to the second replica of the transverse optical phonon-assisted recombination in Si [17, 18]. The broader luminescence features observed at lower energies has previously been ascribed to the Sn-nanocrystals [9] and are also seen in the late-time integrated PL spectra shown in figure 2(b). In this panel, no peak related to Si is observed, demonstrating that the lifetime of the Sn feature is significantly longer than the lifetime of the Si feature. Even though a part of the Sn-related PL extends below the detection limit of 0.76 eV, it is clearly seen that the sample annealed at 725 °C is the most luminescent. This is further elaborated in figure 2(c), which indicates the overall strength of the Sn-related spectral peak.

The Sn nanocrystals have been analyzed by a laser assisted, wide-angle, tomographic atom probe (LaWaTAP) instrument from CAMECA using ultra-violet laser pulses with 343 nm wavelength, 350 fs pulse duration, and 100 kHz repetition frequency and with the samples kept at a temperature of 80 K. A detailed description of this technique can be found in Lefebvre-Ulrikson, *et al* [19]. The tip-shaped specimens, required for APT experiments, were prepared using the standard lift-out method and annular milling procedure [20] in a dual-beam SEM-FIB ZEISS NVision 40 instrument. To prevent the layer of interest from damages, Ga implantation, and amorphization during the sample processing, a 500-nm-thick layer of Pt was deposited on the top of the sample prior to the milling procedure and a low-accelerating voltage (2 kV) was used in the final processing stage. APT is a very local probe, and hence there is a significant risk that any given sample tip contains

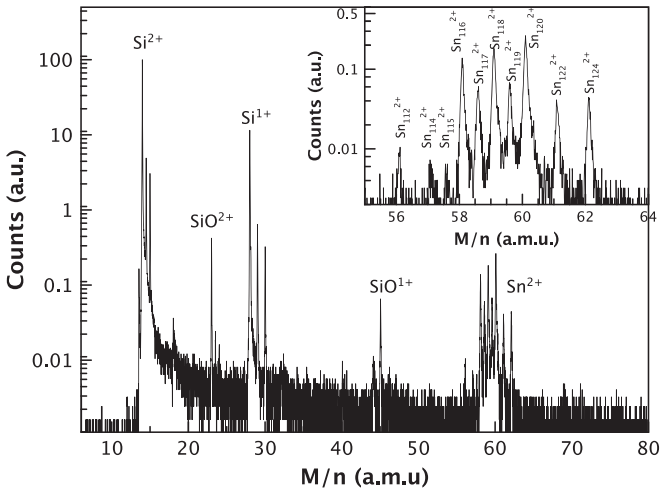

Figure 3. APT mass spectrum obtained from the sample S800-2. The inset shows a magnification of the Sn^{2+} peaks in the 55–64 M/n region.

no nanocrystals, even though it has been prepared from a sample known to contain nanocrystals. For this reason, we have prepared a total of six APT samples, named as S650-1, S725-1, S725-2, S725-3, S800-1, and S800-2, where the first number in each sample name refers to the annealing temperature and the last number to different attempts. Samples S725-1, S725-2, and S800-1 contained no nanocrystals.

A typical mass spectrum obtained during APT experiments of the prepared samples is presented in figure 3. The presence of Si and Sn, constituting the samples, is clearly seen. Silicon is identified in the charged states Si^{2+} and Si^{1+}, whereas tin is detected only as Sn^{2+}. All isotopes of each chemical element (3 for Si and 10 for Sn) are detected in good agreement with their respective relative natural abundances (inset of figure 3). The presence of carbon is indicated by the very weak peaks (M/n = 12 and 40) related to C^{1+} and SiC^{1+} complexes. Some oxygen is detected in the form of SiO ions uniformly across the samples, most likely originating from the growth process or surface oxidation of specimens prepared for APT.

A 3D reconstruction volume related to the APT analysis of the SiSnC layer annealed at 800 °C (S800-2), encapsulated in the Si buffer, is shown in figure 4(a). The regions *I* correspond to the Si buffer and region *II* to the SiSnC layer. It is clearly seen in region *II* that Sn clusters are detected. Figure 4(b) represents the concentration profile for Si and Sn corresponding to the volume in figure 4(a). The Si and Sn content were found to be similar for different samples, and the concentration profile shows that Sn atoms are only located in the SiSnC layers (no diffusion through the Si buffer) with a measured concentration of $X_{Sn} = (1.8 \pm 0.2)\%$, in good agreement with the 1.6% measured previously by second-ion-mass spectrometry [9].

Considering figure 4(a), the SiSnC layer appears rather homogeneous at first glance in the region around the Sn nanocrystals. However, density fluctuations can be difficult to see in a plot containing such a relatively large number of Sn atoms, and for this reason, the Sn distribution will be analyzed more carefully in the following. To this end, define NN1 as the detected nearest-neighbor distance for a given Sn atom as determined directly from the raw APT data, NN2 as the detected distance to the next-nearest neighbor, and so on. These distances will naturally be small in dense regions of Sn and large in more dilute regions. Figure 5 shows histograms of the average distance to the three nearest neighbors, $\langle NN1 + NN2 + NN3 \rangle / 3$. This combination was chosen, on the one hand, to increase the sensitivity to dense regions. It is more likely for this combination than for NN1 alone to take on a low value in dense regions, since it only requires two atoms to statistically form a low value of NN1 in a dilute Sn region. On the other hand, the detection efficiency of the APT procedure is below unity (around 60%), which is the reason for not using the four nearest neighbors that might otherwise appear as an obvious choice given the bonding structure of the Si crystal. The detected location of Sn atoms has a finite measurement precision, and hence the distribution of distances between neighbors will be slightly broadened. In order to avoid edge effects in the histograms of figure 5, care was taken to exclude Sn atoms that were closer than 1 nm from the APT sample surface and from the interface between the SiSnC and Si buffer regions. The histograms show in general two features: firstly, if Sn nanocrystals are present, a small bump appears for mean distances around 0.25 nm characteristic of the bonding length between Sn atoms. This is most pronounced for the sample S800-2, which contains a rather large number of nanocrystals as already shown in figure 4(a). This bump is also quite clear in S650-1 and barely visible in S725-3. Secondly, a broad feature, typically centered around 0.8–1.0 nm, is present for all samples and reflects the properties of the Sn atoms dissolved in the surrounding SiSnC layer. The appearance of this broad feature seems to stand out with a more complex

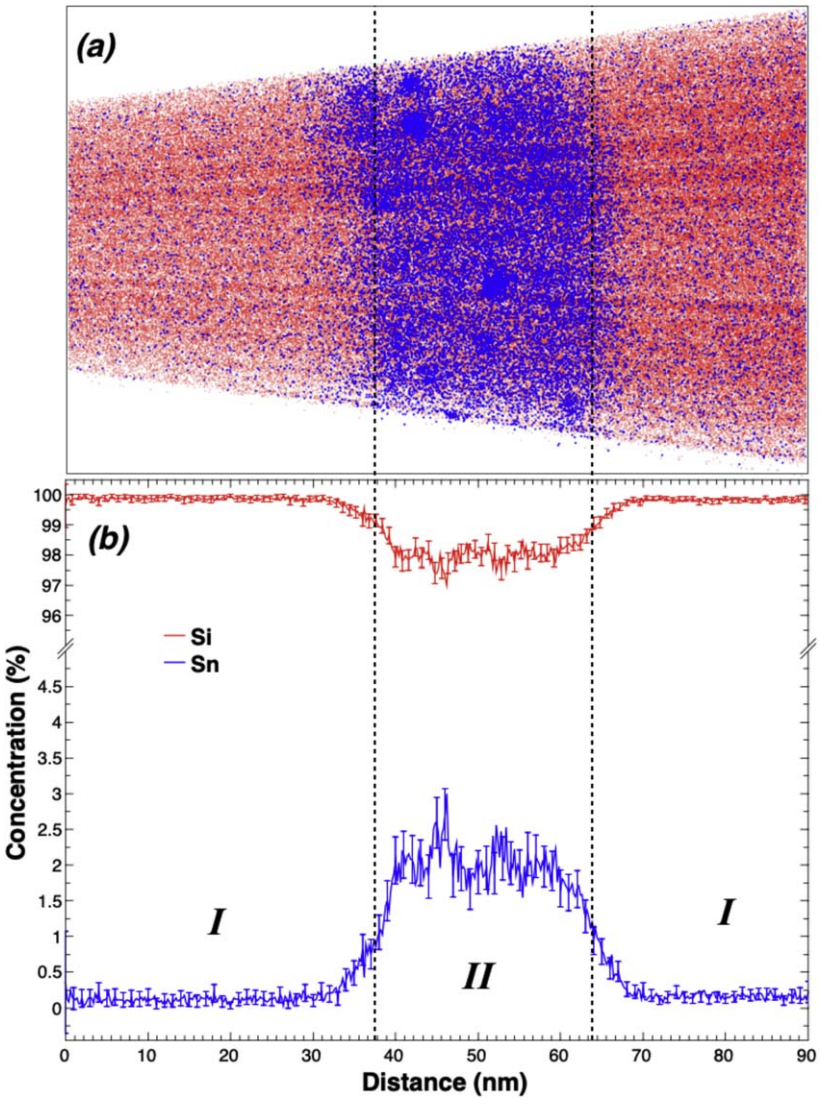

Figure 4. (a) APT reconstruction of the SiSnC layer of volume 52 × 52 × 90 nm^3 for the sample S800-2. (b) Si and Sn concentration profile (in at %) along the 3D sample tip.

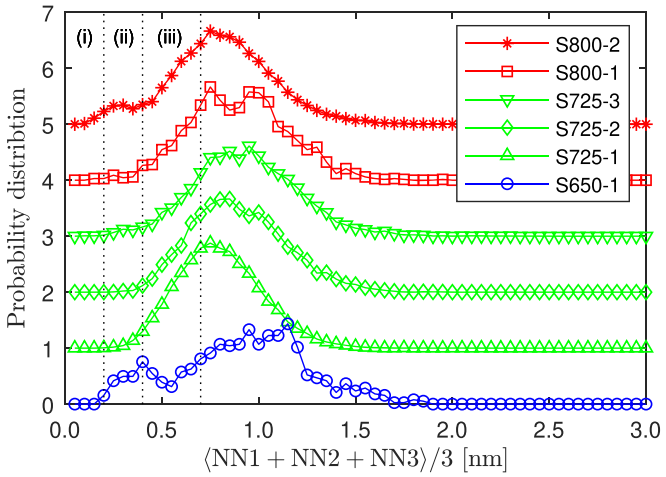

Figure 5. The distribution of the mean distance to the three nearest neighboring Sn atoms for the different APT samples. The graphs are shifted vertically for clarity. The vertical dotted lines separate three ranges in nm as: (i) [0; 0.2], (ii) [0.2; 0.4], and (iii) [0.4; 0.7], which are used for different coloring in figure 6.

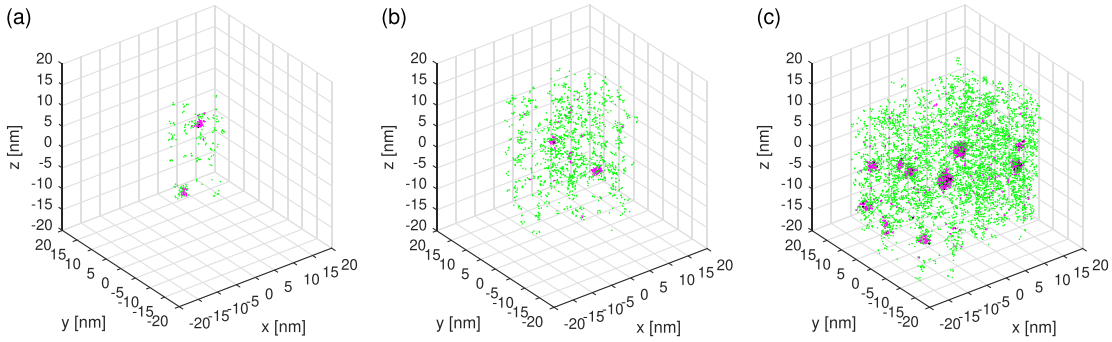

Figure 6. Map of atoms belonging to different regions of the mean distance to the three nearest neighbors. The range of distances, which correspond to the notations (i)–(iii) defined in figure 5, have been plotted with colors: (i) black, (ii) magenta, and (iii) green. The three panels correspond to different APT samples: (a) S650-1, (b) S725-3, and (c) S800-2. Animations of these 3D density fluctuations are available in the Supporting Information.

structure for the two samples S650-1 and S800-1; however, this can be ascribed to a low APT sample volume and therefore poor statistics. Evidently, in some samples the mean distance is smaller than in others. Since the average concentration, X_{Sn}, of Sn atoms is the same for all samples, the variations in the mean neighbor distance corresponds to local variations in the degree to which Sn atoms have segregated towards each other. We wish to remind that the solubility of Sn in Si is $< 0.1\%$, meaning that the solid solution of Sn in the SiSnC layer constitute a meta-stable configuration out of thermodynamic equilibrium. Since the mean distance between Sn atoms appears to be slightly smaller for the S800-1 and S800-2 samples as compared to the S650-1 sample, it is tempting to suggest that Sn atoms have segregated slightly more towards each other for the higher annealing temperature. However, similar differences can be seen between the three samples, S725-1, S725-2, and S725-3, which are all annealed at the same temperature. We thus have to conclude that within the investigated annealing temperature window, there are no detectable variations in the mean nearest-neighbor distance of the dissolved Sn atoms that can be related to temperature effects. The observed difference in the mean neighbor distance for different samples points to spatial variations across the SiSnC layer, which we therefore wish to investigate further.

The vertical dashed lines in figure 5 define the boundary of three chosen regions, (i), (ii), and (iii), of mean distances, which all correspond to quite dense parts of the histograms. The atoms, for which the mean neighbor distance falls within either of these three regions, have been included in the 3D reconstruction plot with different colors in figure 6 for the three nanocrystal-containing samples. In this way, only the Sn nanocrystals (primarily black and magenta) and the most dense part of the Sn solid solution (primarily green) appear. The plots indicate that the solid solution of Sn is located in a columnar structure, which is consistent with the contrast already seen in the STEM images in figure 1. This columnar structure becomes much more evident upon viewing the 3D plots in figure 6 from various angles, and for this reason, animations of the 3D plots are presented for all samples in the Supporting Information. The columns are aligned along the *z*-axis, which correspond to the growth direction. Their typical lateral extent is around 5 nm in all investigated samples, and from figure 1 it is evident that this columnar structure also exists in the as-grown sample. In other words, it must have emerged during the growth process and be independent of the post-annealing temperatures used in this investigation. It should be remarked that the columnar contrast in the STEM images in figure 1 in principle could have had their origin in the STEM specimen milling step. However, the APT has now evidenced that it is really the Sn atoms which are distributed into this columnar variation. No extended defects, like dislocations, stacking faults, or grain boundaries, have been observed from the grown layers using electron microscopy.

Turning towards the Sn nanocrystals, the composition can be measured from APT experiments. Prior to this step, Sn nanocrystals are evidenced and identified using a cluster identification algorithm. As with other techniques working at the atomic scale, APT is subjected to limitations (physical and instrumental). In the present case, a bias exists in the determination of the chemical composition of Sn nanocrystals. Indeed, trajectory aberrations occur for the evaporated atoms from the matrix in the proximity of nanoparticles. In our case, this induces an artificial presence of Si atoms within the Sn nanocrystals. The raw concentration measured on the Sn-nanocrystals from APT analysis is around $X_{Sn} \sim 30$–40 at % in all the samples. However, knowing the APT artefact, we can not directly conclude that Sn nanocrytals are not pure. To determine the real composition, we have applied a correction model [21] based on field evaporation simulations [22]. This model was already applied with success on similar materials [13, 23]. The corrected composition from chemical biases is $X_{Sn} = 100$ at %, i.e. Sn-nanocrystals are pure in Sn with a radius of about 1 nm for all the samples. In other words, the Sn-nanocrystal composition and mean size are not affected by the variations in annealing temperature studied here.

Considering the overall results of the APT analysis in connection to the observed PL, it must be concluded that there is no correlation between the particularly strong PL intensity, observed for the annealing temperature of 725 °C, and the properties offered by the APT analysis, i.e. nanocrystal composition and the level of Sn segregation in the surrounding Si matrix. In fact, based on APT the three investigated samples appear rather similar, which is consistent with previous studies showing that the nanocrystal size distribution does not depend on the annealing temperature within the investigated temperature range [9]. Hence, it seems that the physical mechanism behind the light emission must be sought on the atomic scale from e.g. point defects or complexes of few atoms, possibly located on the nanocrystal surface or within the SiSnC layer. With the present investigation in mind, such atomic complexes would contain Sn and possibly also carbon or oxygen. One could speculate that only one or a few particular types of complexes would lead to light emission and that these just happen to form upon annealing at 725 °C for 20 min. At higher temperatures, these could then evolve further to larger types of complexes that do not give rise to light emission. Light emission has been predicted previously from Sn nanocrystals in the semiconducting α-Sn phase [24]. The recent investigation of the sample annealed at 725 °C, showing it to consist of Sn in the metallic β-Sn phase, adds to the picture that the light emission is not related to the recombination of confined electrons and holes within the Sn nanocrystals.

Acknowledgments

This work was supported by the Villum Foundation.

References

[1] Fang Z, Chen Q Y and Zhao C Z 2013 *Opt. Laser Technol.* **46** 103
[2] Geiger R, Zabel T and Sigg H 2015 *Frontiers in Materials* **2** 52
[3] Oehme M *et al* 2014 *IEEE Photonics Tech. Lett.* **26** 187
[4] Wirths S *et al* 2015 *Nat. Photonics* **9** 88
[5] Al-Kabi S *et al* 2016 *Appl. Phys. Lett.* **109** 171105
[6] Reboud V *et al* 2017 *Appl. Phys. Lett.* **111** 092101
[7] Stange D *et al* 2018 *ACS Photonics* **5** 4628
[8] Huffaker D L, Park G, Zou Z, Shchekin O B and Deppe D G 1998 *Appl. Phys. Lett.* **73** 2564
[9] Roesgaard S, Chevallier J, Gaiduk P I, Hansen J L, Jensen P B, Nylandsted Larsen A, Svane A, Balling P and Julsgaard B 2015 *AIP Adv.* **5** 077114
[10] Roesgaard S, Ramasse Q, Chevallier J, Fyhn J and Julsgaard B 2018 *Nanotechnology* **29** 215707
[11] Arslan I, Yates T J V, Browning N D and Midgley P A 2005 *Science* **309** 2195
[12] Talbot E, Lardé R, Pareige P, Khomenkova L, Hijazi K and Gourbilleau F 2013 *Nanoscale Res. Lett.* **8** 39
[13] Beainy G, Weimmerskirch-Aubatin J, Stoffel M, Vergnat M, Rinnert H, Pareige P and Talbot E 2017 *J. Phys. Chem.* C **121** 12447
[14] Roussel M, Talbot E, Pareige P and Gourbilleau F 2013 *J. Appl. Phys.* **113** 63519
[15] Gaiduk P I, Hansen J L, Larsen A N, Bregolin F L and Skorupa W 2014 *Appl. Phys. Lett.* **104** 231903
[16] Scheffler L, Haastrup M J, Roesgaard S, Hansen J L, Larsen A N and Julsgaard B 2018 *Nanotechnology* **29** 055702
[17] Davies G 1989 *Phys. Rep.* **176** 83
[18] Tsybeskov L and Lockwood D J 2009 *Proc. IEEE* **97** 1284
[19] Lefebvre-Ulrikson W, Vurpillot F and Sauvage X (ed) 2016 *Atom Probe Tomography* (New York: Academic)
[20] Larson D J, Foord D T, Petford-Long A K, Liew H, Blamire M G and Cerezo A 1999 *Ultramicroscopy* **79** 287
[21] Hatzoglou C, Radiguet B, Vurpillot F and Pareige P 2018 *J. Nucl. Mater.* **505** 240
[22] Vurpillot F, Bostel A and Blavette D 2000 *Appl. Phys. Lett.* **76** 3127
[23] Talbot E, Lardé R, Gourbilleau F, Dufour C and Pareige P 2009 *EPL (Europhys. Lett.)* **87** 26004
[24] Jensen R V S, Garm Pedersen T and Pedersen K 2011 *Physica Status Solidi (c)* **8** 1002